Chemical Engineering Journal 496 (2024) 153818

Contents lists available at ScienceDirect

Chemical Engineering Journal

journal homepage: www.elsevier.com/locate/cej

Amphiphilic molecule-assisted perfluoro-alkanes electrolyte for low temperature lithium metal batteries

Jian Qin [a], Yali Zhao [a], Xianjiao Meng [a], Mengfan Wang [a], Zhiping Song [a], Xinping Ai [a,b,*], Hui Zhan [a,b,*]

[a] Hubei Key Lab of Electrochemical Power Sources, College of Chemistry and Molecular Sciences, Wuhan University, Wuhan 430072, China
[b] Engineering Research Center of Organosilicon Compounds & Materials, Ministry of Education, Wuhan University, Wuhan 430072, China

ARTICLE INFO

Keywords:
Low temperature
Weak solvation structure
Perfluorinated electrolyte
Lithium metal batteries
Nonflammable electrolyte

ABSTRACT

Low-temperature working is a big challenge for lithium metal batteries (LMBs), as the efficiency and dendrite growth problems are exacerbated at lower temperature, and meanwhile the impact of slow ion-transfer and difficult ion-desovation is intensified. Herein, the amphiphilic effect of hydrofluoroether was revealed, and fully utilized to construct a nonflammable perfluoro-alkanes electrolyte. With the well-regulated Li^+ solvation and the purposedly tuned SEI, the electrolyte brought highly reversible Li deposition from − 60 °C to 60 °C. As a result, Li/$LiFePO_4$ cell (1.5 mAh cm^{-2}) with thin Li anode presented ultra-long cycling life. The work supplies a new design concept for low-temperature LMBs electrolyte.

1. Introduction

Rechargeable lithium (Li)-ion batteries often play an indispensable role in various fields [1,2]. Nowadays, the mainstream Li-ion battery founded on intercalation chemistry have achieved great success, either in electronics, electric vehicle field or new-energy industry, and material/technology innovation has been occasionally proposed. However, the traditional Li-ion battery industry has recently being confronting much more challenge, as the requirement on energy density as well as the climate adaptability continuously increased [3–5]. Under this scenario, over the past decade, we have witnessed accelerated progress toward the ultimate goal of Li metal battery. The high specific capacity (3860 mAh g^{-1}), low redox potential (−3.04 V vs. standard hydrogen electrode and none-intercalation kinetics of Li anode all contribute to the glorious future of Li metal battery [6–8]. However, the merits meanwhile become the obstacles in the practical application. Highly reducible Li potentially supplies a high voltage output, it also generates a series of intertwined issues, like the low coulombic efficiency (CE), dendrite growth, short lifespan and even shortcut risk. Unlike the well-established solid electrolyte interphase (SEI) protection in Li-ion batteries, the plating/stripping redox of Li anode significantly complicates the formation and maintenance of a uniform and mechanically robust interface on Li [9–11]. The heterogeneous and fragile SEI is not able to effectively shield Li metal, instead, it exacerbates Li deposition issues.

In view of classical electrochemistry, the transmission across SEI is just an intermediary stage between the ion-diffusion in liquid zone and ion reduction in bulk electrode. However, within the Li reduction kinetics, in many cases, SEI quality is actually an underlying determinant of cell failure, because this interface guides the ion-flux between the electrolyte and the anode, isolates the newly formed Li from corrosive electrolyte and copes with the local stress generated during Li deposition/dissolution [12–14]. The role of SEI makes it highly susceptible to both the electrolyte “above” it and the Li deposition “beneath” it. Such susceptibility can be vividly reflected by the SEI formed spontaneously in carbonate electrolytes. The formed organic-rich SEI layer, with low Young’s modulus and shear modulus, is so fragile and cannot well adapt to the so-called “infinite” volume fluctuation during Li plating/stripping. Under the dual influences of dramatic stress change and dendrite growth preference of Li, crack-generation and crack-repairing process recurs throughout the whole cell service [15–17]. Based on this widely-observed phenomenon and widely accepted recognition, it is evident that constructing an interface using a regulated organic/inorganic mixture can minimize the contact between Li metal and the electrolyte, thereby reducing parasitic side reactions and stabilizing Li-metal. [18]. Accordingly, particular inorganic SEI components, such as LiF, Li_3N or Li_2O is marked because their high Young’s modulus and interfacial energy can reinforce the SEI “wall” against the impact from both sides [19–23]. Additionally, their weak interaction with Li can reduce their

* Corresponding authors.
E-mail addresses: xpai@whu.edu.cn (X. Ai), zhanhui3620@126.com (H. Zhan).

https://doi.org/10.1016/j.cej.2024.153818
Received 5 April 2024; Received in revised form 16 June 2024; Accepted 5 July 2024
Available online 6 July 2024
1385-8947/© 2024 Elsevier B.V. All rights are reserved, including those for text and data mining, AI training, and similar technologies.

mutability and the reactivity toward Li, thus strengthen the intrinsic robustness of SEI. Among these valued inorganic SEI components, LiF is a pivotal role as its production can be adjusted within a wide range, from few percentages in standard carbonate electrolyte to a dozen of percentage in designed electrolyte. More importantly, it has super high mechanical strength (Young's modulus value ranging from 50 to 140 GPa) [24], and its poor ion-conductivity can shield the ion-flow toward the dendrite, thus reduce the Li-deposition on tip and dendrite propagation. Its effectiveness is evidenced by comparing the Li-deposition coulombic efficiency (CE) in 2 M $LiNO_3$ + triglyme (G3) and 2 M LiTFSI + G3 electrolyte (**Fig. S1**). The former electrolyte can produce totally LiF-free SEI, it did not bring highly reversible and stable Li^+ reduction as being expected, although physical characterization showed that appreciable Li_3N which is Li^+-conductive and has high Young's modulus was contained in SEI. In general, the function of LiF has been summarized as promoting the formation of chunky and less-dendritic Li through "Tip shielding effect", suppressing continuous electrolyte decomposition and then improving the Li-deposition CE, additionally, its wide electrochemical stability window, negligible solubility in most electrolytes as well as the ability to regulate surface tension has also been highlighted [25,26].

A feasible way to increase the LiF percentage in SEI is to increase the decomposition of electrolyte anion, as most Li salt is fluorine-containing and capable of producing LiF. Many novel design concepts have been generated accordingly [27–32], including highly concentrated electrolyte (HCE), localized highly concentrated electrolyte (LHCE) and weakly solvating electrolyte (WSE), they all can supply more LiF by the decomposition priority of fluorinated-rich anions in the inner solvation structure of Li^+. Among the applicable lithium salts, lithium bis(fluorosulfonyl) imide (LiFSI) has received extensive attention, mainly because that the SO_2-F bonds in FSI^- is weaker than the C − F bonds in $TFSI^-$ or P − F bonds in PF_6^-, and it is more readily to break and produce LiF [33]. Alternate approach is to use electrolyte containing fluorinated-rich co-solvent to optimize the formation process of LiF in SEI layer. If retrieving the information about the solvents in Li-secondary battery, we can see a gradually increased application of fluorinated solvent. From early-used common fluoro-esters (e.g., Fluoroethylene carbonate (FEC) that has a high anodic-stability) to recently proposed fluoro-ethers/-esters (e.g., bis(2,2,2-trifluoroethyl) ether (BTFE), methyl 2,2,2-trifluoroethyl carbonate (FEMC) that participates in the LiF formation), we can clearly see a trajectory from low-fluorine to high-fluorine and from strong polarity to weak polarity [34–37]. Nowadays, the representative fluorinated-rich and weak polar solvent, hydrofluorinated ether (HFE) has demonstrated the effectiveness in various Li-metal secondary battery. It inspires the exploration of other fluorine solvent. A good example is perfluorinated alkane, the O (atom)-free and completely saturate structure renders it with even weaker polarity and/or even higher fluorine content. However, this series of solvent usually presents "extreme" inertness, and cannot be miscible with the commonly used solvent, thus their application till now is seldom mentioned.

In this work, an amphiphilic molecule-assisted perfluoro-alkane electrolyte was proposed for the first time. Mixture solvent was designed according to the electrostatic matching principle [38]. Amphiphilic ether of 1,1,2,2-tetrafluoroethyl 2,2,3,3-tetrafluoropropyl (TTE) assisted the non-polar 2-perfluoromethylpentane (FMP) mixing with strong-polar 2-methyltetrahydrofuran (THF2), and finally constructed a perfluoro-characteristic electrolyte. Relatively stronger-polar THF2 dissolved lithium salts and constituted the inner layer of Li^+-solvation shell within which the anion content could be purposedly regulated by the amount of THF2. Non-polar FMP not only physically reduced the viscosity and freezing point of electrolyte but also chemically regulated the Li^+ solvation structure, LiF formation and SEI quality. Additionally, it enhanced the anti-oxidation resistance of the electrolyte and imparts a completely nonflammable feature. The weak-polar TTE was utilized to fuse strong polar THF2 and non-polar FMP through the amphiphilic-characteristic electrostatic potential in the molecular surface. As a proof-of-concept, the rationally designed electrolyte had high ionic conductivity, low desolvation energy over a wide range of temperature and excellent flame retardancy. More importantly, it brought uniform Li plating and very reversible Li plating/stripping from 60 °C to − 40 °C (e.g., CE values of 99.21 % at 60 °C, 99.65 % at 30 °C and 99.14 % at − 40 °C). With this electrolyte, the Li/$LiFePO_4$ cells (1.5 mAh cm^{-2}, Li excess 2.6 ×) achieved 95 % capacity retention after 380 cycles at − 20 °C, and the Li/NCM622 cell could work at − 60 °C with 80 mAh g^{-1} capacity release.

2. Results and discussion

2.1. Electrolyte design and solvation structure characterization

Molecular polarity, as an essential property, it very much determines the miscibility of solvents, and such dependence deduces the "like dissolves like" law. Its quantization usually depends on the analysis of electrostatic potential (ESP) on the surface and the symmetry of electron distribution, additionally, the dipole moment parameter is usually viewed as a useful and referential index. According to quantum chemistry theory, when two solvents interact with each other, electrostatic interaction can occur on the molecule surface where electrostatic potential has the equal amplitude but opposite sign ($|ESP_{min}| \approx ESP_{max}$) [38]. If the interaction is sufficiently stronger than the molecular cohesion, the so-called miscibility can be observed as the consequence of mutual delamination. In the study (Fig. 1**a**), perfluoroalkane (FMP) is a typical non-polar molecule as quantum computation indicates that its dipole moment is as low as 0.15 Debye, and fluorine atoms uniformly snatching the charge of carbon atoms brings a not-high ESP_{max} and very small $|ESP_{min}|$ (Fig. 1**b**) [39]. THF2 molecular, with the dipole moment of 1.65 Debye, has much stronger polarity, and negative charges concentrating on the oxygen atoms results in large $|ESP_{min}|$ and relatively smaller ESP_{max}. Thus, if FMP being mixed with THF2, electrostatic interaction between them will be theoretically impossible because of the "huge" gap between the unmatched ESP_{max} and $|ESP_{min}|$. TTE, though usually being known for its weak-polarity, it actually has not-low dipole moment (1.48 Debye). Additionally, the − CF_2 − segments partially snatches the negative charge that should have concentrated on the oxygen atom, and it bring an increase in the ESP_{min} value (namely from the − 1.44 eV for cyclic ether THF2 to − 0.71 eV for fluoro-ether TTE), as well as ESP_{max} (1.38 eV for TTE versus 0.51 eV for THF2). Consequently, A wonderful "indirect ESP matching" between THF2 and FMP is attained through the very appropriate ESP value of TTE (specifically, $^{THF2}|ESP_{min}| \approx {}^{TTE}ESP_{max}$ and $^{TTE}|ESP_{min}| \approx {}^{FMP}ESP_{max}$ (**Table S1**)). The ESP value of TTE theoretically classifies it as an "amphiphile" molecule. Such amphiphilicity was experimentally validated by the dissolution test in Fig. 1**c**. We saw that mixing FMP and THF2, the mixture was stratified into upper and lower layers, while in FMP + TTE, THF2 + TTE as well as FMP + TTE + THF2 mixture, homogeneous and transparent solution was observed. More proofs were supplied by the nuclear magnetic resonance (NMR) measurement (**Fig. S2**). The two dimensional 1H-19F heteronuclear overhauser effect spectroscopy (1H-19F HOESY) [40] confirmed the affinity of TTE to THF2 and FMP. In the mixture of THF2 + TTE, a strong interaction between the H atom in THF2 and F atom in TTE was probed. Likewise, in the mixture of TTE + FMP, the interaction between the H atom of TTE and F atom of FMP was traced.

Molecule polarity also deeply affects the solvent dissolving salt. In the general cognition that Li salt dissolution requires polar solvent, ESP is a crucial factor, specifically, a sufficiently negative ESP_{min} of the solvent, coordinating with the positively charged Li^+ ions, fundamentally contributes to the driving force of salt dissociation and salt dissolution [39,41]. For example, the solvent of acetonitrile (AN) with $|ESP_{min}| > ESP_{max}$ is the "good solvent" for Li salt, while the solvent of dichloromethane (DCM) with $|ESP_{min}| < ESP_{max}$ is viewed as the "antisolvent" for Li salt. For the same reason, in our study, we observed that THF2 could well dissolve LiFSI, while FMP and TTE could not

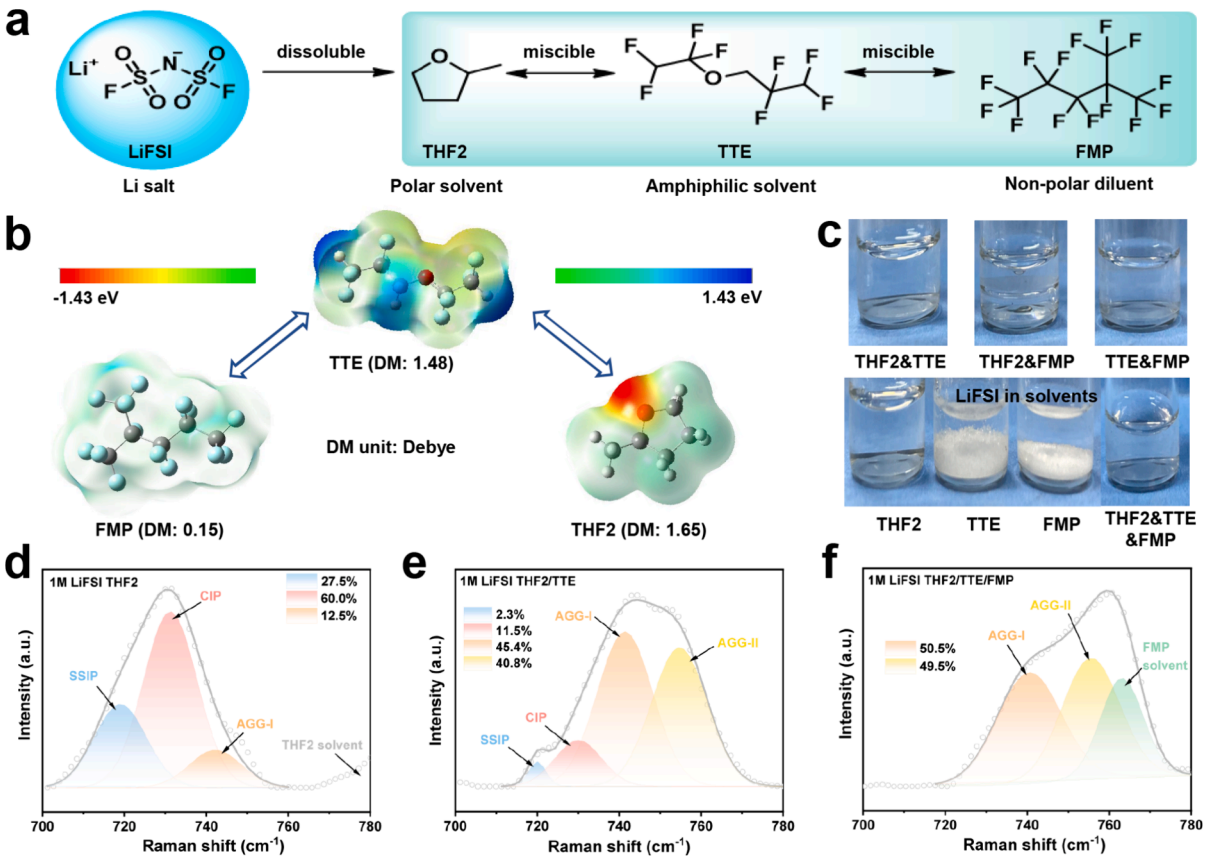


Fig. 1. Illustration of the amphiphilicity of TTE and characterizations of the electrolyte solvation. (a) Molecule structures of polar THF2, amphiphilic TTE, nonpolar FMP, and a sketchy description of their intercalation. (b) Electrostatic potential maps and dipole moment of different solvent molecules. (c) Visual observation of the miscibility between solvents and the dissolution of Li salt in THF2, TTE, FMP and THF2 + TTE + FMP mixture solvent. (d-f) Raman spectra of LiFSI electrolyte with THF2, THF2 + TTE and THF2 + TTE + FMP solvent at 25 °C. Color scheme of atoms: C, grey; H, white; O, red; F, cyan. Notes: the peaks of 763.1 cm^{-1} and > 770 cm^{-1} originate from FMP and THF2 respectively.

(Fig. 1**c**). But after fusing FMP and THF2 by TTE, the mixture solvents became a "good solvent" for LiFSI.

Certainly, the effect of amphiphilic TTE and thus-formed perfluor-solvent is much more than the simple dissolution assistance, it profoundly influences the environment around Li^+ and alters the solvation structure. In the ^{7}Li NMR spectra in **Fig. S3**, we noticed that comparing with 1 M LiFSI THF2, partially replacing THF2 by TTE led to an obvious upfield shift. The observation suggested that in 1 M LiFSI THF2/TTE electrolyte, more FSI^- approached Li^+ and shielded the Li^+ nuclei. In 1 M LiFSI THF2/TTE/FMP electrolyte, more upper field shift was observed as more FSI^- in the neighborhood of Li^+. Raman spectroscopy further proved the evolution of solvation structures. As shown in Fig. 1**d-f**, the signals between 700 ~ 780 cm^{-1} are from the vibrations of the S-N-S bond in FSI^-, and its variation has been commonly used as an indicator of the binding between Li^+ and FSI^- in the electrolyte [42,43]. The peak of 763.1 cm^{-1} originates from FMP (**Fig. S4**), and the peaks around 720 cm^{-1}, 731 cm^{-1}, 741 cm^{-1}, and 754 cm^{-1} usually are assigned respectively to solvent-separated ion pairs (SSIP), contact ion pairs (CIP) and ion aggregates-I (AGG-I, that is FSI^- entering the inner layer of Li^+ solvation) and AGG-II (that is FSI^- being adjacent to Li^+ in the inner solvation sheath) [44,45]. A tendency was clearly revealed that with the THF2 solvent being replaced by THF2 + TTE binary solvent then THF2 + TTE + FMP ternary solvent, the proportion of AGG-type FSI^- continuously increased, especially in LiFSI THF2 + TTE + FMP electrolyte, $_{AGG\text{-}II}FSI^-$ became a dominant species.

The spectral characterization proved that more FSI^- participated in Li^+-solvation in TTE and FMP-containing electrolyte, and a detailed solvation structure was given by theoretical computation. Density functional theory (DFT) calculation (**Fig. S5**) showed that the interaction force between THF2 and Li^+ was stronger than Li^+-TTE and Li^+-FMP, indicating in 1 M LiFSI THF2/TTE/(FMP) electrolyte, most solvation force was provided by THF2. Classical molecular dynamics (MD) simulation (Fig. 2**a**) further revealed the evolution of solvation structure when the second and the third solvent being introduced. The radial distribution function (RDF) data from MD simulation (Fig. 2**b**) showed that 1 M LiFSI in THF2 displayed a characteristic solvent-separated ion pair (SSIP) structure, in which the Li^+ coordination was dominated by THF2 molecules. The average coordination number was 2.11 in Li^+-$(THF2)_m$ and 2.81 in Li^+-$(FSI^-)_n$. When THF2 being partially replaced by TTE, the *m* value decreased to 1.64 accompany with *n* value increasing to 2.96 in 1 M LiFSI THF2/TTE electrolyte. More FSI^- entered into the solvation inner layer and formed a characteristic contact-ion pair (CIP) structure. When the third solvent of FMP was introduced, *n* value further increased to 3.04 and *m* value was lowered to 1.49 in 1 M LiFSI THF2/TTE/FMP electrolyte, and FSI^- became the dominant species in the solvation sheath. Based on the solvation structure obtained in MD simutation, the DFT was used to calculate the Li^+ desolvation energy of THF2-based electrolyte and FMP-based electrolyte, and the results showed that the latter had lower desolvation energy (**Fig. S6**). The variation in solvation structure directly affected the ion-diffusion. An interesting change in Li^+ diffusion was revealed by the mean square displacement (MSD) analysis. In Fig. 2**c**, the calculated Li^+ diffusion coefficient was 0.89 × 10^{-7} cm^2 s^{-1} in 1 M LiFSI THF2/TTE and 4.81 × 10^{-7} cm^2 s^{-1} in 1 M LiFSI THF2 electrolyte, and it was understandable as the weakened solvation reduced the salt dissociation. However, Li^+ diffusion coefficient did not further diminish in 1 M LiFSI THF2/TTE/

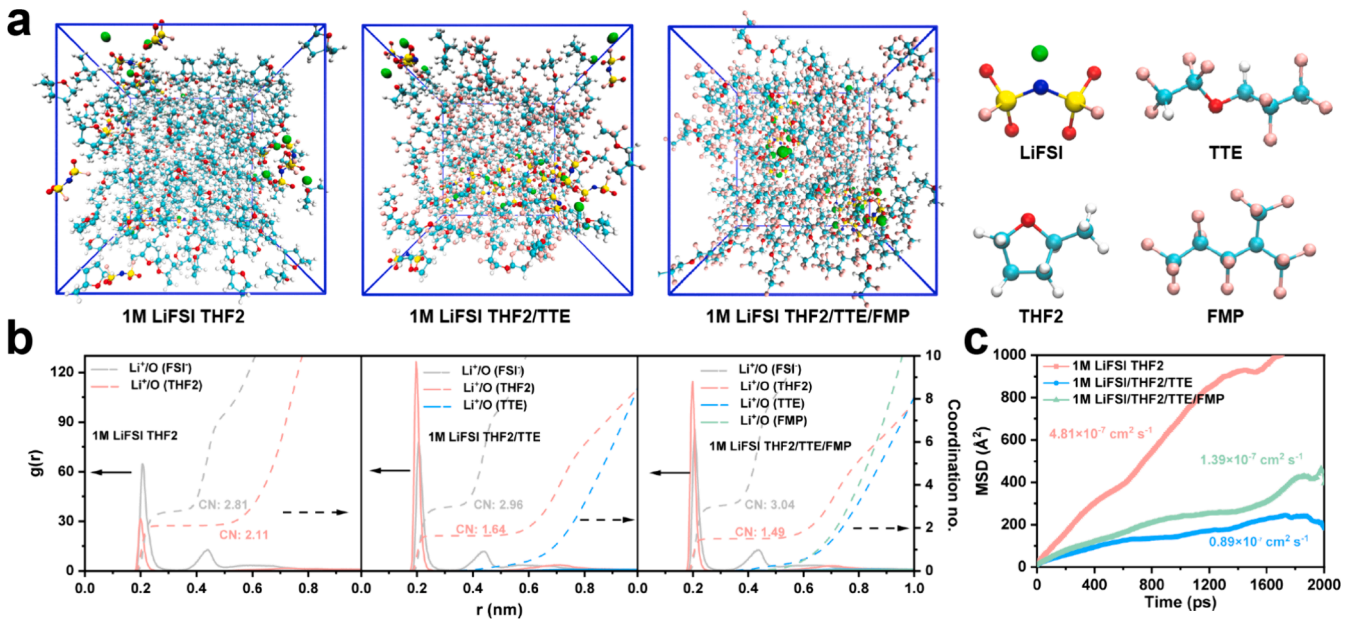


Fig. 2. Theoretical analysis of electrolyte structure. (a) Snapshot, (b) Li^+ radial distribution function (RDF) and (c) Mean square displacement (MSD) curves obtained from MD simulations of 1 M LiFSI THF2, 1 M LiFSI THF2/TTE and 1 M LiFSI THF2/TTE/FMP.

FMP electrolyte (1.39×10^{-7} cm^2 s^{-1}) even more FSI^- was incorporated into the solvation shell, and this result was basically consistent with the observation in ^7Li diffusion ordered spectroscopy (DOSY) (Fig. S7). It might be explained by that FMP-adding reduced the viscosity (Table S2) and it in turn enhanced the Li^+ diffusion capability.

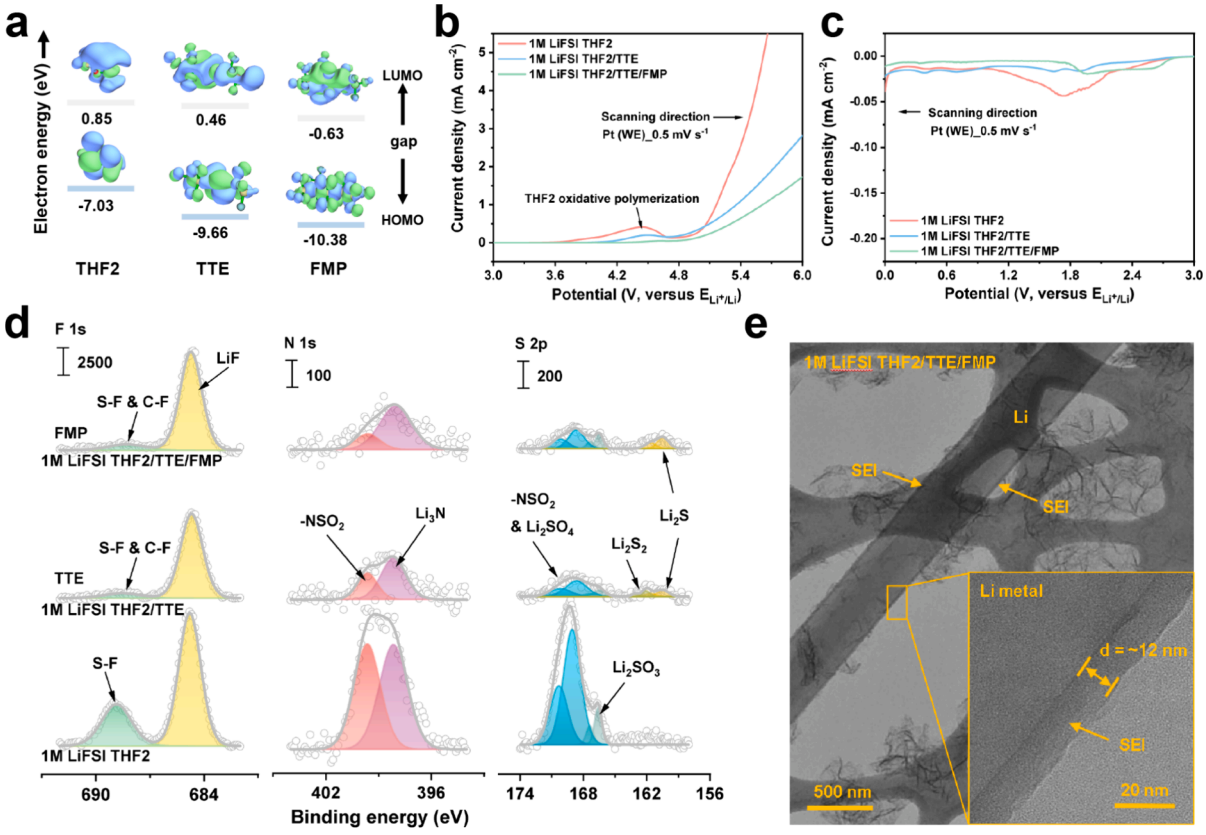


Fig. 3. Electrochemical stability of different electrolytes and spectroscopy characterization of the SEI formed during Li deposition in different electrolytes. (a) HOMO/LUMO energy level of THF2, TTE and FMP molecule. The (b) anodic and (c) cathodic window of different electrolytes. (d) XPS analysis [11,13–15,26,33] of the interface formed during Li deposition in different electrolytes of 1 M LiFSI THF2, 1 M LiFSI THF2/TTE and 1 M LiFSI THF2/TTE/FMP. (e) Cryo-TEM images of Li deposition on Cu grid in 1 M LiFSI THF2/TTE/FMP electrolyte (inset: zoomed view of the selected-area) [46].

2.2. Effects of perfluoro-alkanes electrolyte on SEI

Besides altering the solvation structure, the solvents also directly influence the mass transfer across SEI as the SEI conductivity highly depends on the species generated from electrolyte decomposition. The highest occupied/lowest unoccupied molecule orbit (HOMO/LUMO) energy level of the solvents was calculated as they fundamentally reflected the oxidation/reduction resistance. In Fig. 3**a,** we noticed that from THF2 to TTE then FMP, the HOMO energy decreased, suggesting the stronger oxidation resistance of FMP. It partially explained the observation obtained in the anodic scanning of electrolytes in which the 1 M LiFSI THF2/TTE/FMP electrolyte presented highest anti-oxidation voltage (Fig. 3**b**). Likewise, the minimum LUMO energy of FMP was also reflected in the cathodic scanning of 1 M LiFSI THF2/TTE/FMP electrolyte. Appreciable cathodic current was observed at 2.6 V, corresponding to the decomposition of FMP, then another cathodic peak appeared at 1.9 V, indicating the subsequent reduction of FSI^- in the inner Li^+-solvation shell, after that, no considerable current was observed (Fig. 3**c**). The result suggested that the earlier-formed LiF effectively passivated the electrode interface and suppressed the continuous decomposition of electrolyte. By contrast, the cathodic current of 1 M LiFSI THF2 electrolyte was much larger though it initiated at more negative potential, additionally, we found after the FSI^- decomposition at around ~ 1.85 V, many more cathodic peaks appeared at lower potential, indicating the continuous electrolyte decomposition. The cathodic scanning curve obtained in 1 M LiFSI THF2/TTE was similar to 1 M LiFSI THF2 electrolyte, but the current was much smaller. We further analyzed the surface chemistry on Li metal that had been cycled in the Li/Li cells with different electrolyte in term of X-ray photoelectron spectroscopy (XPS). The F 1 s, N 1 s and S 2p spectra was supplied in Fig. 3**d,** and the atomic percentage was calculated and presented in **Fig. S8**. The most notable difference was the ratio between the organic species and inorganics. Specifically, the − SF or − CF signals were quite appreciable in 1 M LiFSI THF2, but it was much weakened in 1 M LiFSI THF2/TTE and barely observed in 1 M LiFSI THF2/TTE/FMP. On the other side, in 1 M LiFSI THF2, the incomplete reduction product of FSI^-, such as − NSO_2 (~400.1 eV), −CF/−SF (~688.9 eV) and Li_2SO_3/Li_2SO_4 (~169.2 eV) was the dominant species, while in 1 M LiFSI THF2/TTE, their proportion considerably decreased. Furthermore, in 1 M LiFSI THF2/TTE/FMP, these signals were further weakened and were largely replaced by the energy binds of some complete reduction product, like LiF (684.7 eV), Li_3N (398.1 eV) and Li_2S_2/Li_2S (~160.8 eV). The observed difference was consistent with the result obtained in Fig. 3**c**, and it could be explained by that more FSI^- in the solvation shell increased its decomposition, and the earlier FMP and FSI^- decomposition made it more readily be deeply reduced as the solvent reduction was

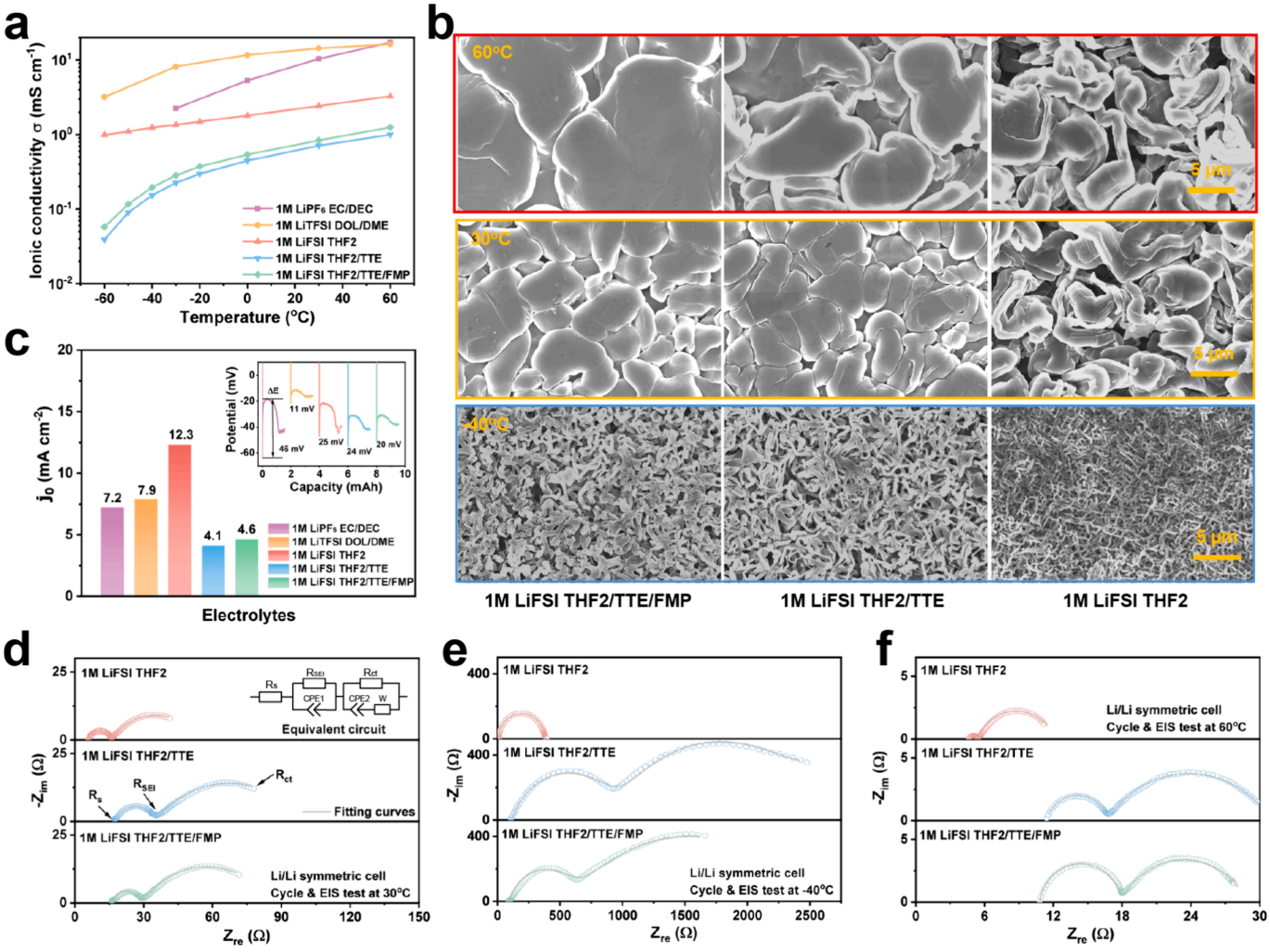


Fig. 4. Morphology characterization and kinetics analysis of Li deposition. (a) The dependence of ionic conductivity on temperature in different electrolytes. (b) SEM images of Li deposition on Cu substrate in different electrolytes at 60 °C, 30 °C and − 40 °C, 1 mAh cm^{-2}Li was loaded on Cu foil at a current density of 0.5 mA cm^{-2}. (c) Exchange current density of Li^+ reduction in different electrolytes, and the insets showed the lithium deposition curves in 2nd cycle. (d-f) Comparison of impedance diagrams of Li/Li cells obtained in different electrolytes after cycled 5 times at (d) 30 °C, (e) − 40 °C and (f) 60 °C, respectively.

suppressed by the early-formed inorganic shield with poor electron-conductivity. The reduced solvent decomposition directly led to the formation of a thinner SEI which was verified by high-resolution cryogenic transmission electron microscopy (cryo-TEM). Li was electrochemically deposited on Cu grid in different electrolytes. In the 1 M LiFSI THF2/TTE/FMP electrolyte, the formed SEI had a uniform thickness of approximately 12 nm **(**Fig. 3**e).** While in 1 M LiFSI THF2 and 1 M LiFSI THF2/TTE electrolyte, thicker and less-uniform SEI (~36 nm in the former and 17 ~ 22 nm in the latter) was obtained (**Fig. S9**).

2.3. Kinetics analysis of Li deposition

In the above, the effect of perfluo-characteristic electrolyte on solvation and SEI composition was independently investigated without accounting for other interferences, such as temperature. We further investigated the effect of the electrolyte on the whole Li^+ reduction kinetics. The first stage in Li^+ reduction kinetics, mass transfer in liquid zone, was analyzed in term of conductivity measurement, in which the solvation effect on ionic dynamics could be directly reflected by the ion-conductivity. In Fig. 4**a**, commercial ester and ether electrolytes (1 M $LiPF_6$ EC/DEC and 1 M LiTFSI DOL/DME) had an order of magnitude higher conductivity than the others, but due to the freezing of 1 M $LiPF_6$ EC/DEC at − 60 °C, valid data could not be obtained. 1 M LiFSI THF2/TTE/FMP and 1 M LiFSI THF2/TTE electrolyte exhibited a lower ion-conductivity in the temperature range from 60 °C to − 60 °C, it was understandable as the much poorer solvation force of TTE and FMP reduced the salt dissociation and decreased the amount of movable ion. Among them, 1 M LiFSI THF2/TTE/FMP presented higher conductivity than 1 M LiFSI THF2/TTE electrolyte, well agreeing with the higher Li^+ diffusion coefficient obtained in MD simulations. Despite the FMP-containing electrolyte has smaller conductivity than commercial ester electrolyte, the > 0.2 mS cm^{-1} conductivity at − 40 °C can meet the requirement of practical application.

Secondly, the morphology of Li deposition was compared and it was more influenced by the last reaction stage in Li^+ reduction. 1 mAh cm^{-2}Li was loaded on Cu substrate in different electrolyte under 0.5 mA cm^{-2} current density prior to the morphology observation. Different electrolyte leading to different Li deposition was visually displayed in **Fig. S10**. From 60 °C to − 40 °C, only in 1 M LiFSI THF2/TTE/FMP electrolyte, Li deposition was always evenly adhered to Cu substrate, and in other electrolytes, at either − 40 °C or 60 °C, incomplete Li coverage on Cu was observed (at − 40 °C, uniform Li deposition could not be formed in 1 M $LiPF_6$ EC/DEC, 1 M LiTFSI DOL/DME and 1 M LiFSI THF2, while at 60 °C, we failed to obtain a uniform Li deposition in 1 M LiFSI THF2/TTE). SEM observation supplied more detail. The deposited Li became smaller with the temperature decreasing in commercial electrolyte (**Fig. S11**) and studied electrolyte **(**Fig. 4**b).** The tendency was much more remarkable when using 1 M $LiPF_6$ EC/DEC. Additionally, this commercial electrolyte also led to the most inferior Li deposition quality. For example, very ununiform particle size and rod-like morphology was observed at 60 °C and 30 °C, and at − 40 °C, mossy-like morphology was observed. 1 M LiFSI THF2/TTE/FMP electrolyte brought the most uniform and densest Li deposition. When it being used as electrolyte, round-shape and bloke-like Li deposition with quite bigger particle size (>10 μm) was obtained at 60 °C or 30 °C, even at − 40 °C, the homogeneous particle size distribution (~ μm particle dimension) and closely packed Li deposition was maintained. Similar observation was gained in the cross-section pictures that was taken on Cu substrates with 2 mAh cm^{-2}Li loading (**Fig. S12**). The thinnest Li-deposition layer of 37 μm was produced in 1 M LiFSI THF2/TTE/FMP, indicating the densest Li deposition. The results demonstrate that the electrolyte has very profound effect, its influence extends far beyond the ion-transfer or ion-solvation in bulk electrolyte and SEI formation, and reaches the end of the kinetic process. To explain why 1 M LiFSI THF2/TTE/FMP provides so many benefits, we retrieved the whole Li^+ reduction process, and tried to answer the question with the aid of electrochemical measurements.

In the classical electrochemical kinetics theory, ion-diffusion and ion-reduction are regarded as the determining step in cathodic process. The ion-reduction, in another word, electron-gain step, its kinetics character is usually indexed by initial exchange current density (j_0). In the knowledge of Li^+-reduction kinetics [47,48], it is widely accepted that too-high j_0 (indicative of much quicker electron-gain) and slow cation flux is the root cause for the dendrite growth. The j_0 values were acquired from the cyclic voltammetry (CV) measurement and Tafel fitting (Li/Cu cells was used in the CV test and Cu microelectrode with Φ = 126 μm was the working electrode to minimize the voltage error, **Fig. S13**). It should be noted that, here the mentioned j_0 is an apparent value as the electron-gain step cannot be totally isolated from the precedent Li^+-desolvation, Li^+-FSI^- dissociation, and even has a subtle relation with the SEI species, but the comparison is still meaningful as it has been made under the identical condition. As shown in Fig. 4**c**, the TTE and TTE/FMP-containing electrolytes brought small j_0 (namely 4.1 mA cm^{-2} and 4.6 mA cm^{-2} respectively), which were mainly due to the decreased activity of Li^+ caused by incomplete dissociation of the salt. They were significantly lower than that obtained in 1 M LiFSI THF2 electrolyte (12.3 mA cm^{-2}), suggesting that 1 M LiFSI THF2 electrolyte would lead to much quicker $Li^+ \rightarrow Li$, and dendrite growth would be more likely to occur in it. Meanwhile, compared to 1 M LiFSI THF2/TTE electrolyte, 1 M LiFSI THF2/TTE/FMP electrolyte brought improved kinetics, and it could be explained by the generation of high-quality SEI (Fig. 3**e**, **Fig. S9**). More information was given by the nucleation overpotential measurement (inset in Fig. 4**c**), we found that comparing with FMP-free electrolyte (1 M LiFSI THF2 and 1 M LiFSI THF2/TTE electrolyte), 1 M LiFSI THF2/TTE/FMP electrolyte brought a relatively lower nucleation overpotential (20 mV), which could be explained by more LiFSI decomposition generating more lithium-philic site (e.g., Li_3N) on the electrode surface. On the other side, considering that much thinner SEI was formed in 1 M LiFSI THF2/TTE/FMP, the interface resistance should be correspondingly smaller, thus it could be inferred that when Li plating occurred in this electrolyte, the influence of ion-transfer in liquid zone was appreciable as there was a significant gap between the nucleation overpotential and the overall Li-deposition overpotential (31 mV, represented by the plateau voltage).

The inference was proved by the electrochemical impedance spectroscopy (EIS) measurement that was conducted on Li/Li symmetric cells after being cycled 5 times at 30 °C, −40 °C and 60 °C in the THF2-containing electrolytes. As shown in Fig. 4**d-f**, all the impedance diagrams presented a typical two-half-circle character, representing Li^+ diffusing across SEI then reducing on the electrode surface. Besides, in 1 M LiFSI THF2/TTE and 1 M LiFSI THF2/TTE/FMP electrolyte, the electrolyte resistance was considerable, consistent with their smaller ion-conductivity. With the temperature decreasing from 60 °C to − 40 °C, the total cell resistance, including solution resistance (R_s), charge transfer resistance (R_{ct}) and mass transfer resistance across SEI (R_{SEI}) all increased, no matter what kind of electrolytes was used. Among them, the resistance obtained in 1 M LiFSI THF2 electrolyte was the lowest (**Table S3**), it should be explained by that the much smaller Li sediment actually increased the surface area and decreased the real current density. If comparing 1 M LiFSI THF2/TTE with 1 M LiFSI THF2/TTE/FMP electrolyte, at 30 °C and − 40 °C, the cell using 1 M LiFSI THF2/TTE/FMP electrolyte showed a lower R_s, R_{ct} as well as R_{SEI} than that using 1 M LiFSI THF2/TTE. In **Fig. S14,** Arrhenius fitting of the R_{ct} values was conducted and "activation energy" was calculated, the results showed that the 1 M LiFSI THF2/TTE/FMP electrolyte exhibited the lowest activation energy (39.82 kJ/mol) for Li^+ reduction. These results again demonstrated that FMP improved Li^+-reduction kinetics, and improvement was originated from FMP-induced higher j_0 and thinner or more conductive SEI. Certainly, we also noticed that at 60 °C, higher R_{SEI} was obtained in 1 M LiFSI THF2/TTE/FMP than 1 M LiFSI THF2/TTE electrolyte, it might be caused by the SEI deterioration under high temperature, after all the boiling point of FMP is only 58 °C (see **Table S2**).

Now, the effect of THF2/TTE/FMP ternary solvent could be clearly elucidated. The primary solvent of TTE has weak polarity, it fuses the polar solvent of THF2 and non-polar FMP, and their combination significantly increases the participation of FSI^- in the solvation and promotes its decomposition during the cathodic process. Hence, the initially produced LiF (from FMP and FSI^- decomposition) effectively and appropriately passivates the surface, reducing the decomposition of other solvent. The resulting thinner SEI inhibits the dendrite growth due to the high mechanical strength and ion-shielding effect of LiF, additionally, another decomposition product, Li_3N, promotes ion-transmission across the SEI (**Fig. S15**). More importantly, the Li-deposition pattern is altered because of the tuned j_0. For these reasons, 1 M LiFSI THF2/TTE/FMP electrolyte is able to well address the efficiency and dendrite growth issues in Li secondary battery, and moreover, it can enhance the cycling life of Li secondary battery and make it better adapt to the low-temperature condition.

2.4. Effect of electrolyte on Li plating/striping behavior

The effect of electrolyte as well as temperature on Li plating/striping was investigated in term of Li/Li symmetric cells and Li/Cu half-cells. Firstly, average coulombic efficiency (CE) was measured on Li/Cu cells according to the protocol described in reference [49]. Very poor average CE was obtained in commercial ester electrolyte of 1 M $LiPF_6$ EC/DEC and ether electrolyte of 1 M LiTFSI DOL/DME in the temperature range from 60 °C to − 20 °C (**Fig. S16a-c**), the efficiency could not surpass 97 %, and it shrank dramatically with temperature deceasing. At − 40 °C (**Fig. S16d**) or − 60 °C (**Fig. S16e**), even one Li plating/stripping cycle could not be completed smoothly. The result was consistent with previous report [50,51]. By contrast, in Fig. 5**a**, the studied electrolytes all brought higher and more stable efficiency. Among them, highest efficiency as obtained in 1 M LiFSI THF2/TTE/FMP (~99.65 %) while lowest one was observed in 1 M LiFSI THF2 (~98.04 %) at 30 °C. Such electrolyte-efficiency relation was observed again at − 20 °C (Fig. 5**b**), −40 °C (Fig. 5**c**) and − 60 °C (**Fig. S17a**). On the other side, similar to that observed in **Fig. S16**, even using the studied electrolytes, lower temperature also caused efficiency shrinkage. For example, in 1 M LiFSI THF2/TTE, the CE decreased from 99.31 % at 30 °C to 99.24 % at − 20 °C then 98.76 % at − 40 °C and 89.97 % at − 60 °C. The lower temperature brough more significant impact if 1 M LiFSI THF2 electrolyte was used, and micro-short circuit occurred early when the temperature dropped below − 40 °C, indicating the dendrite issue was aggravated at low temperature. Furthermore, the SEI formed in 1 M LiFSI THF2 electrolyte was not sufficiently strong to handle this

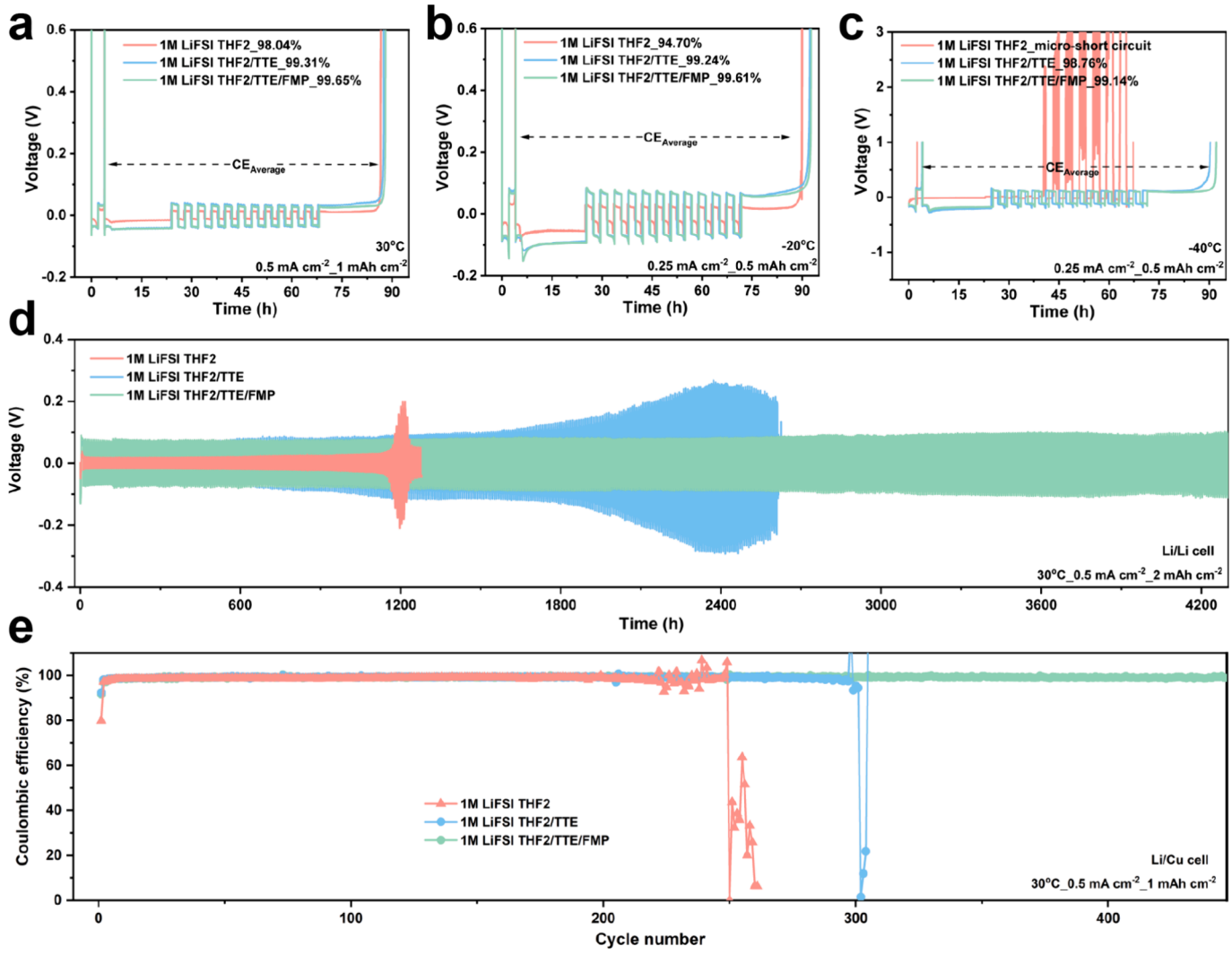


Fig. 5. Li plating/stripping in different electrolytes. Average CE measured on Li/Li symmetric cells at (a) 30 °C with the current density of 0.5 mA cm^{-2} and the cutoff capacity of 1 mAh cm^{-2}, (b) − 20 °C and (c) − 40 °C with the current density of 0.25 mA cm^{-2} and the capacity of 0.5 mAh cm^{-2}. (d) Cycling life of Li/Li symmetric cells at 30 °C under the current of 0.5 mA cm^{-2} and 2 mAh cm^{-2} capacity limit. (e) Cycling tests of Li/Cu half-cells using the current density of 0.5 mA cm^{-2} with the capacity limit of 1 mAh cm^{-2} at 30 °C.

challenge. In comparison, the efficiency was much better reserved in 1 M LiFSI THF2/TTE/FMP, as high as 99.14 % and 90.63 % were obtained at − 40 °C and − 60 °C, respectively. A phenomenon was noticed that in 1 M LiFSI THF2/TTE and 1 M LiFSI THF2/TTE/FMP electrolytes, when the temperature was up to 60 °C, the CE was slightly smaller than 30 °C (Fig. S17**b**), it very possibly was caused by SEI dissolution or deterioration.

Step-wise cycling tests were conducted to evaluate the influence of current on Li deposition. In Fig. S18, the Li/Li cells were cycled at 30 °C under gradually increased current from 0.2 mA cm^{-2} to 4 mA cm^{-2}, the Li/Li cell with 1 M LiTFSI DOL/DME, or 1 M LiFSI THF2 presented smaller overpotential. TTE-containing electrolyte brought relatively larger polarization. The polarization disparity between 1 M LiTFSI DOL/DME and 1 M LiFSI THF2/TTE/(FMP) increased along with the current increasing, and the overpotential obtained in 1 M LiFSI THF2/TTE/FMP electrolyte was 260 mV at 4 mA cm^{-2}, almost 3 times higher than that obtained 1 M LiTFSI DOL/DME. However, the small-overpotential advantage of 1 M LiTFSI DOL/DME or 1 M LiFSI THF2 electrolyte could not be well maintained as short-cut quickly occurred. In the long-term cycling test, the initially smaller overpotential observed in the Li/Li cells with 1 M LiTFSI DOL/DME and 1 M $LiPF_6$ EC/DMC could not be sustained after hundreds of cycles due to short circuit fault (Fig. S19). The studied electrolytes all brought improved cycling stability, and in 1 M LiFSI THF2/TTE/FMP electrolyte, the Li/Li cell could cycle for more than 4300 h with a well-maintained overpotential of ~ 75 mV (Fig. 5**d**). At − 40 °C (Fig. S20), the low temperature significantly impacted the cycling life. The Li/Li cell using 1 M LiFSI THF2 and LiTFSI DOL/DME both malfunctioned within one hundred hours. However, in the case of 1 M LiFSI THF2/TTE/FMP, the Li/Li cell could cycle for thousands of hours (>3200 h).

The benefit of FMP was corroborated in the cycling test of Li/Cu cell. Since no additional Li source is included in the working electrode, dead-Li accumulation and efficiency-related Li exhaustion becomes immediately evident through cell failure. We saw that either at 30 °C (Fig. 5**e** and Fig. S21**)** or − 40 °C (Fig. S22), the cell using 1 M LiFSI THF2/TTE/FMP electrolyte presented much more stable cycling and much longer

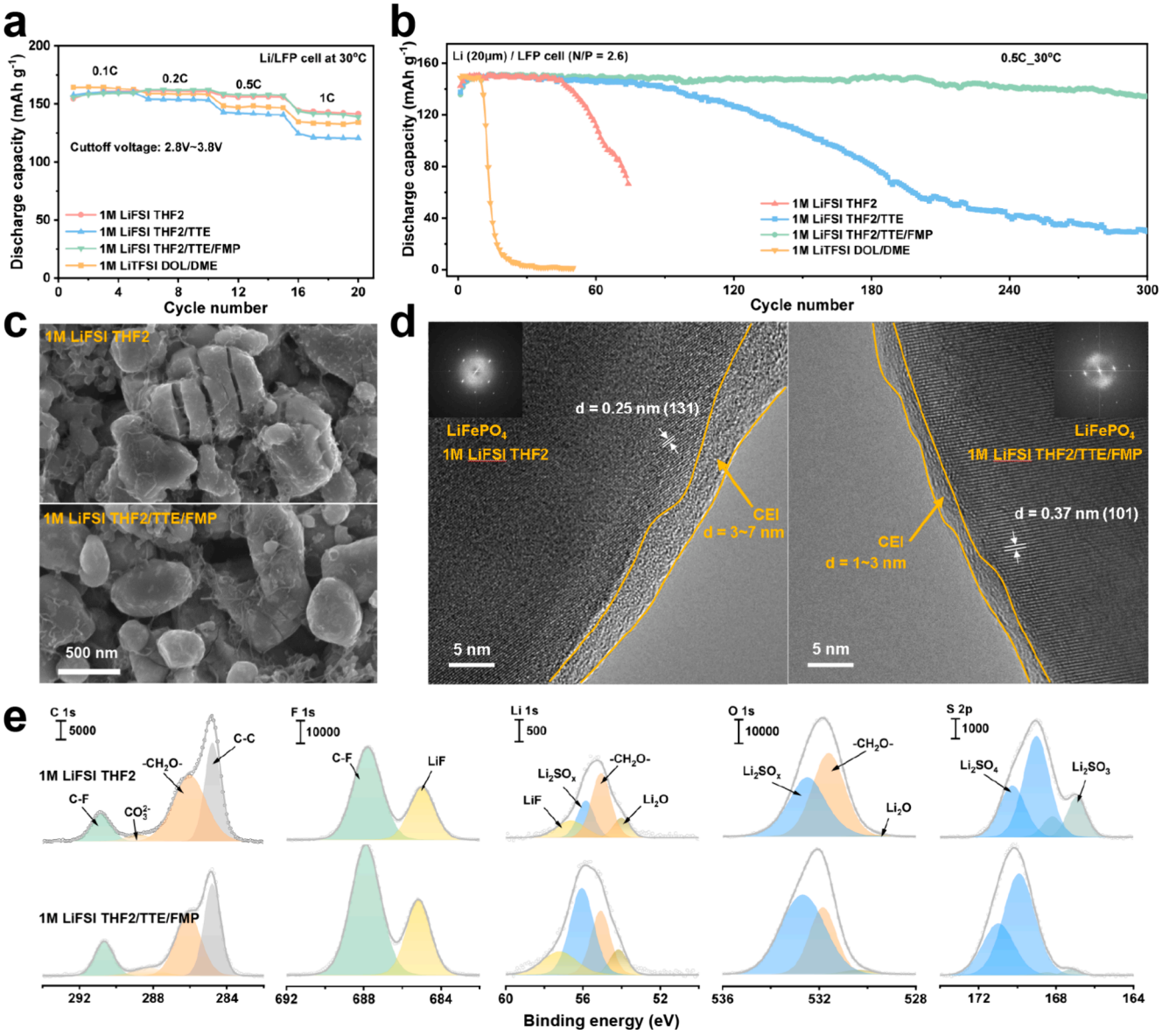


Fig. 6. Electrochemical performance and interface analysis of Li/$LiFePO_4$ cell. (a) Rate performance and (b) long-term cycling of Li/$LiFePO_4$ cell in different electrolytes at 30 °C. The full cells consisted of a 20 μm Li foil anode and $LiFePO_4$ cathode with the areal capacity of 1.5 mAh cm^{-2}, and they were charged and discharged between 2.8 V and 3.8 V at 0.5C-rate (1C = 1.5 mA cm^{-2}). Comparison of (c) SEM, (d) TEM images and (e) XPS spectra acquired form the $LiFePO_4$ cathode cycled in electrolytes of 1 M LiFSI THF2 and 1 M LiFSI THF2/TTE/FMP.

cycling time. Additionally, the voltage profiles in Fig. S23 further indicated that stable polarization was an important reason for the enhanced cycling stability. In 1 M LiFSI THF2/TTE, the polarization enlarged by eight times at ~ 280th cycle, then cell failure occurred at the ~ 298th cycle. Unlike it, slightly changed polarization was observed in 1 M LiFSI THF2/TTE/FMP electrolyte even after 400 cycles. These results suggested that the non-polar perfluoro-alkane (FMP) solvent did play an essential role in the Li^+-reduction kinetics, it much influenced the solvation structure, reduced the de-solvation barrier, and altered interfacial chemistry, promoting block-like Li deposition. With the assistance, highly reversible Li^+ deposition/dissolution was achieved in the 1 M LiFSI THF2/TTE/FMP electrolyte across a wide temperature range.

2.5. Effect of electrolyte on Li/$LiFePO_4$ full cell

After confirming the benefit of the 1 M LiFSI THF2/TTE/FMP electrolyte for Li plating/striping, it was employed in a Li/$LiFePO_4$ (Li/LFP) full cell with a cathode loading of 10 mg cm^{-2} (corresponding to the areal capacity of 1.5 mAh cm^{-2}). Firstly, the rate capability of Li/LFP full cells was tested because of the concern that FMP-adding might increase the Li^+ deposition polarization. The result was quite unexpected, as the bigger overpotential generated on Li anode did not much affect the capacity release. On the contrary, after the formation cycles, the Li/LFP cell using 1 M LiFSI THF2/TTE/FMP electrolyte presented slightly higher discharging capacity than those using FMP-free electrolyte when the current varied from 0.1C to 1C (Fig. 6**a**). If comparing with the 1 M LiFSI THF2/TTE electrolyte, the capacity advantage could be maintained even when the current rate was increased to 5C (**Fig. S24**). The impact of current was better reflected by the voltage profiles in **Fig. S25**. We saw that, even up to 142 mAh g^{-1} capacity being released in 1 M LiFSI THF2/TTE/FMP at 1C, the reduction in energy output was non-negligible. This was evident as the voltage gap between charging and discharging plateau was wider than that observed with the 1 M LiFSI THF2 electrolyte. Upon further comparison of the initial stage in the discharging process, we found that the bigger electrolyte resistance, or in another word, the smaller ion-conductivity of 1 M LiFSI THF2/TTE/FMP should be blamed, as the voltage drop occurred predominantly at the beginning of discharging.

Long-term cycling was conducted under 0.5C at 30 °C, and a 20 μm Li foil was used as anode (Fig. 6**b**). 1 M LiFSI THF2/TTE/FMP electrolyte led to the most stable cycling, namely, 89 % capacity retention after 300 cycles, superior to other electrolytes. When a thicker lithium foil (40 μm) was used (**Fig. S26**), the cycling life of the Li/LFP cell could be further extended to 900 cycles, with 89 % of the capacity being retained. In addition, the coulombic efficiency of the cell using the 1 M LiFSI THF2/TTE/FMP electrolyte remained consistently near 100 % throughout the cycling test. The observation suggested that a stable interface was successfully constructed and maintained, significantly reducing Li consumption. On the other side, the enhanced oxidation-resistance of the 1 M LiFSI THF2/TTE/FMP electrolyte should also be highlighted, as it could alleviate the electrolyte decomposition on cathode side. In **Fig. S27 and** Fig. 6**c,** we compared the SEM images of fresh LFP electrode and the cycled ones. Generally, in 1 M LiFSI THF2 electrolyte, the particle integrity could not be well preserved, and after 250-times cycling, microcracks was found, and could be more clearly observed in the magnified SEM (Fig. 6**c).** In contrary, if the LFP cathode being cycled in the 1 M LiFSI THF2/TTE/FMP electrolyte, the electrode morphology barely changed and particle breakage was seldom observed. Obviously, the difference in electrode/particle integrity should be explained by the more effective CEI built in 1 M LiFSI THF2/TTE/FMP electrolyte, and it was evidenced in Fig. 6**d.** The high-resolution TEM showed that very thin (1 ~ 3 nm) and uniform CEI was formed in 1 M LiFSI THF2/TTE/FMP electrolyte on the surface of LFP, while in 1 M LiFSI THF2, the thickness of surface layer varied from 3 ~ 7 nm. The difference indicated that similar to SEI, the CEI quality was also highly dependent on electrolyte. The surface chemistry on LFP cathode was analyzed in term of XPS measurement. The comparison in Fig. 6**e** and **Fig. S28** revealed that the CEI formed in 1 M LiFSI THF2/TTE/FMP was more enriched in inorganic species, such as LiF/Li_2SO_x. In contrast, in the 1 M LiFSI THF2 electrolyte, organic species ($-CH_2O-$) constituted a significant proportion of the CEI. It was understandable as the oxidation resistance of electrolyte was greatly strengthened by FMP and it helped to produce a more robust inorganic CEI protective layers.

Given the low melting point of the solvents and the facile Li^+-desolvation in the 1 M LiFSI THF2/TTE/FMP electrolyte, we can have high expectations for its low-temperature performance. Fig. 7**a and Fig. S29** compared the low-temperature discharging capacity of Li/$LiFePO_4$ cells in different electrolytes, and the results showed that the capacity delivered in the 1 M LiFSI THF2/TTE/FMP electrolyte was comparable to that in 1 M LiTFSI DOL/DME or 1 M LiFSI THF2 electrolytes. Additionally, much higher capacity was delivered in 1 M LiFSI THF2/TTE/FMP electrolyte than 1 M LiFSI THF2/TTE at − 40 °C, as FMP increased the conductivity and Li-deposition kinetics. Observing the evolution of the voltage profile (Fig. 7**b**), we noticed that the capacity gradually decreased, and the voltage polarization gradually enlarged as the temperature dropped. Impedance analysis revealed that the slower electrochemical kinetics was responsible for the increased polarization (Fig. 7**c**). Lower temperature not only slowed down the ion-migration within electrolyte, it also led to sluggish kinetics, or in another word, increased cell-resistance (represented by the half-circle in the impedance plot, including mass transfer across SEI/CEI, reaction kinetics of the bulk electrode). As LFP cathode has not-good low-temperature tolerance and moderate rate capability, the Li/LFP full cell was cycled at − 20 °C under a 0.1C rate. More than 380 times stable cycling was obtained in 1 M LiFSI THF2/TTE/FMP electrolyte (Fig. 7**d**), while in 1 M LiFSI THF2, Li was quickly exhausted at the ~ 80th cycle. In 1 M LiFSI THF2/TTE, despite Li being available, dendrite growth led to a short-cut and cell failure at the 245th cycle. Besides, 1 M LiFSI THF2/TTE/FMP electrolyte was compatible with high voltage cathode material (4.5 V) and had obvious antioxidant advantages compared to the other two electrolytes (**Figs. S30, S31**). Hence the Li/NCM622 full cell also presented appreciable discharging capacity at − 20 °C (135 mAh g^{-1}) and − 40 °C (88.4 mAh g^{-1}). If the temperature dropped to − 60 °C, the cell could still be charged /discharged normally under 0.01C-rate. The application of the 1 M LiFSI THF2/TTE/FMP electrolyte can be extended to Li metal organic batteries. In **Fig. S32,** the Li/polyimide (Li/PI5) full cell could well reserve the capacity either at 30 °C or − 20 °C.

Another notable merit of LiFSI THF2/TTE/FMP electrolyte is the nonflammability. Adding amphiphilic TTE in LiFSI THF2 electrolyte could quickly extinguish the fire, and if further adding FMP, the LiFSI THF2/TTE/FMP electrolyte became totally nonflammable (**Fig. S33, Table S4**). Thus, even dendrite growth accidently occurred, the cell safety could be guaranteed.

In summary, the LiFSI THF2/TTE/FMP electrolyte well addressed the SEI issues and difficult-desolvation problem in Li-metal secondary. With the assistance of perfluoro-like electrolyte, robust SEI was built during Li deposition and it significantly improved the Li plating/striping efficiency and extended the cycling life of Li/Cu half-cell and Li/LFP full cell. However, we must acknowledge that there is a trade-off for achieving such excellent properties. Despite the deliberately regulated solvent ratio, the relatively lower ion conductivity of the LiFSI in THF2/TTE/FMP electrolyte significantly contributes to increased polarization. This is evident from the larger overpotential observed in Li/Cu or Li/LFP cells. It is conceivable that if the power capability is the primary requirement at low temperature, 1 M LiFSI THF2/TTE/FMP may not be an optimal choice. Meanwhile, we have to recognize that all-weather (−60 °C ~ 60 °C) Li-metal battery is still a huge challenge as some irreconcilable contradictions were involved in the electrolyte/electrode design. Firstly, currently, achieving rapid ion migration in the liquid zone and quick desolvation over a wide temperature range through electrolyte design remains challenging. This is because smooth Li^+

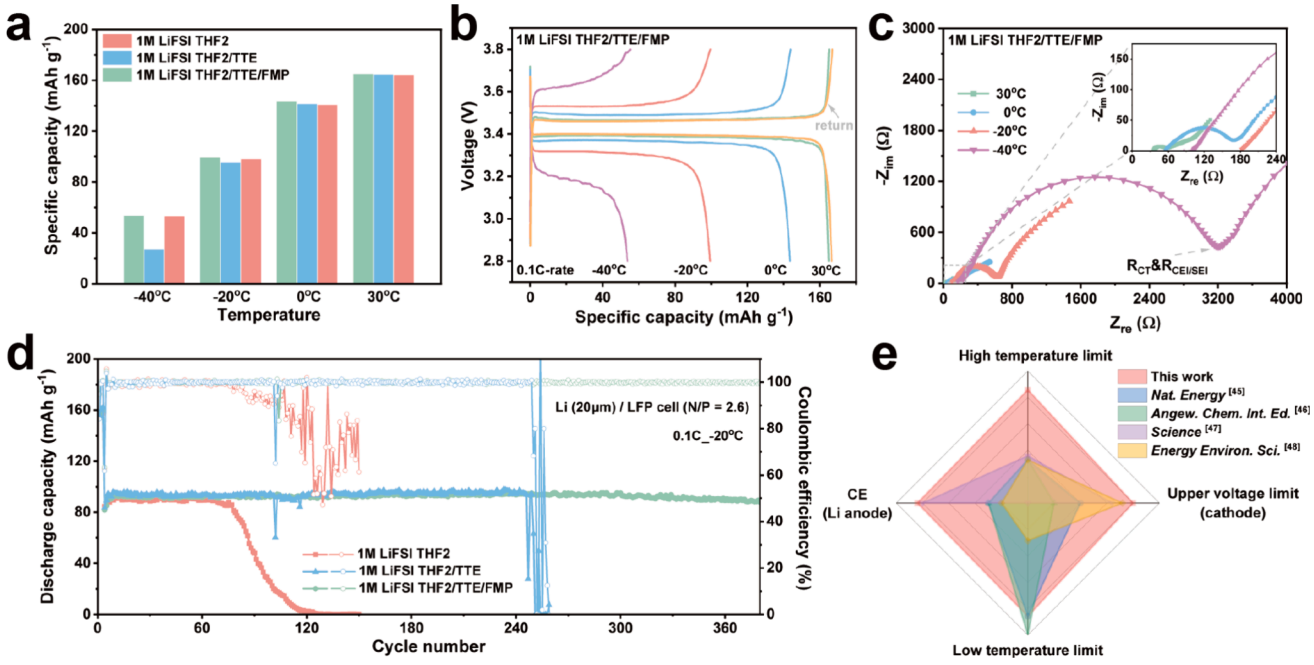


Fig. 7. Low temperature performance of Li/$LiFePO_4$ full cell. (a) Capacity comparison of Li/$LiFePO_4$ full cells using different electrolytes in the temperature range from − 40 °C to 30 °C. (b) Voltage profiles and (c) electrochemical impedance of the Li/$LiFePO_4$ cell using 1 M LiFSI THF2/TTE/FMP electrolyte at varied temperature. (d) Long-term cycling of the Li/$LiFePO_4$ cells in 1 M LiFSI THF2, 1 M LiFSI THF2/TTE, and 1 M LiFSI THF2/TTE/FMP electrolyte at − 20 °C under 0.1C. (e) Comparison of our work with some typical state-of-art electrolyte [52–55], the comparison was made according to the data reported in the references in **Table S5**.

transfer within the electrolyte requires sufficient salt dissociation driven by solvation forces. However, stronger solvation forces often correspond to difficult desolvation. Thus, we saw the weak solvation strategies (including diethyl ether and fluoromethane), could achieve reversible Li reduction/oxidation at low temperatures, but similar to our work, it resulted in lower ion-conductivity and might damage the power performance. Secondly, inconsistent and even conflicting requirements are imposed on the electrolyte design. To be specifically, the all-weather battery theoretically requires the using of solvent with wide liquid-zone, but such solvent usually has a strong coordination with Li^+, which in turn leads to poor low-temperature performance, typical examples are PC and EMC. Thus, even the ether-containing low-temperature electrolyte brought robust SEI, high efficiency and satisfying low-temperature kinetics, the continuous operation in high-temperature environment is still problematic as electrolyte evaporation or possible thermal instability must be considered. In **Fig. S17b**, we saw that if the Li/Li half-cell with the optimum 1 M LiFSI THF2/TTE/FMP electrolyte being cycled at 60 °C, the average CE slightly decreased comparing with that obtained at 30 °C. On the other side, when cycling the Li/LFP full at 60 °C, 50-times stable cycling was achieved in the 1 M LiFSI THF2/TTE/FMP electrolyte, which outperformed other electrolytes used for comparison. However, we still observed a gradual capacity decay after the 50th cycle. High temperature-resulted electrolyte loss was proved as the reason. In **Fig. S34**, we observed that refilling electrolyte into a "dead" Li/LFP cell could totally restored its functionality. Thirdly, the electrode compatibility, especially cathode compatibility is still an insurmountable obstacle to all-weather electrolyte. In this work, reversible Li plating/striping was achieved at quite low temperature, and even a practical Li/LFP full could run at − 40 °C, however we cannot ignore a fact that the ether-containing electrolytes often exhibit poor oxidation resistance, hence incorporating them into the mainstream Li-secondary battery with high-voltage cathode becomes challenging. Moreover, it is very difficult to realize the all-weather Li-metal secondary battery by tackling the issues in sequence as highly intertwined kinetics factors/parameters are involved. For example, highly concentrated or locally concentrated electrolytes could much improve the efficiency at room temperature, expedite the desolvation and help to form mechanically strong SEI, but the high CE could not be well maintained if low temperature was applied. In other cases, the mixture solvent of fluoroether + linear ester could support the low- temperature working of the cell and it was compatible with most cathodes, but the relatively smaller efficiency would inevitably bring Li consumption in a long-term cycling.

In Fig. 7**e** and **Table S5**, a comparison between our work and recent advances in the low temperature electrolyte for Li metal batteries was made from three dimensions, including CE, lower/higher working-temperature limit and cathode compatibility. Though without the most distinguished low-temperature performance, the 1 M LiFSI THF2/TTE/FMP electrolyte did bring highest Li^+-reduction efficiency and enable a wide cathode compatibility and wide working temperature zone. Additionally, the concept or the mechanism of utilizing amphiphilic TTE to fuse polar THF2 and none-polar FMP can be extended to many other electrolyte systems, and the broad applicability has been already proved by a complementary experiment in which 1 M LiFSI THF2/TTE/MP (Methylpentane) electrolyte was made and it also brought very reversible Li plating/stripping (**Fig. S35**).

3. Conclusion

In summary, we have demonstrated the amphiphilic effect of TTE and it can be utilized to fuse THF2 and its antisolvent of FMP, thus prepared perfluoro-characteristic electrolyte with ternary solvent has desirable solvation structure and can improve the SEI quality and much enhance the Li reduction efficiency. Meanwhile, the introduction of FMP fluothane increases the high-voltage tolerance of the electrolyte and reduces the safety risks. Optimized 1 M LiFSI THF2/TTE/FMP electrolyte enabled the Li/$LiFePO_4$ cell work within a wide temperature range from − 40 °C to 60 °C, and it also led to an ultra-long cycling life of Li/$LiFePO_4$ cell with thin Li anode. The wide compatibility of the electrolyte was exemplified by 4.5 V Li/NCM622 cell. This work represents a significant advancement in low-temperature batteries, it also provides a new design concept for the LMB electrolyte with good temperature adaptability and safety protection function.

4. Experimental section

4.1. Preparation of materials

Battery-grade electrolytes of 1 M $LiPF_6$ EC/DEC (1/1, v/v) and LiTFSI DOL/DME (1/1, v/v) were purchased from Zhangjiagang Guotai Huarong New Chemical Materials Co., Ltd. The $LiFePO_4$ (~1.5 mAh cm^{-2}) and NCM622 (~1.7 mAh cm^{-2}) cathodes were purchased from Guangdong Canrd New energy Technology Co., Ltd. Thick Li disc (400 μm) and ultra-thin Li foil (20 μm) were bought from China Energy Lithium Co., Ltd. Lithium bis(fluorosulfonyl) imide salt (LiFSI, 99.9 %, water ≤ 100 ppm, Dodochem), 2-Methyltetrahydrofuran (THF2, 99 %, water ≤ 50 ppm, Adamas), 1,1,2,2-tetrafluoroethyl 2,2,3,3-tetrafluoropropyl ether (TTE, > 98 %, Adamas), 2-Perfluoromethylpentane (FMP, 99 %, TCI) and Methylpentane (MP, > 99 %, Adamas) were used directly without further purification. For 1 M LiFSI THF2 electrolyte, 1 mmol LiFSI was dissolved in 1 mL THF2. For 1 M LiFSI THF2/TTE electrolyte, 1 mmol LiFSI was dissolved in THF2/TTE mixed solvents (0.2 mL/0.75 mL, v/v). For 1 M LiFSI THF2/TTE/FMP electrolyte, 1 mmol LiFSI was dissolved in THF2/TTE/FMP mixed solvents (0.2 mL/0.625 mL/0.125 mL, v/v). Electrolytes preparation was performed in a glove box ($O_2 \leq 0.1$ ppm, $H_2O \leq 0.1$ ppm) filled with Ar atmosphere at ambient temperature.

4.2. Theoretical calculations

Based on the density functional theory in the Gaussian 16 software package [56–58], the B3LYP/6–311++G(d,p) (geometry optimization and frequency computation) and B3LYP/ma-def2-TZVP (single point energy calculation) was selected to calculate HOMO-LUMO energy levels, electrostatic potential (ESP) of solvents, ion–solvent binding energy and ionic desolvation energy. Molecular dynamics (MD) simulations were performed in the GROMACS 2021 software package [59] to investigate the coordination structures of solvents, cations and anions in different electrolytes. Density functional theory (DFT) calculations using the Gaussian 16 package [60] based on the hybrid functional B3LYP functional and 6–311 g(d,p) basis functions along with the gd3bj dispersion correction, were used to determine the atom charge of FSI^-, THF2, TTE and FMP molecules. The OPLSS-AA force field [61] and MKTOP [62] were used to parametrize all atoms, such as the bond parameters, angle parameters and the dihedral angles, and so on. For electrolyte structure determination, #1 simulation box containing 20 LiFSI and 200 THF2 molecules corresponded to 1 M LiFSI THF2 electrolyte, #2 simulation box containing 20 LiFSI, 40 THF2 and 100 TTE molecules corresponded to 1 M LiFSI THF2/TTE electrolyte, and #3 simulation box containing 20 LiFSI, 40 THF2, 80 TTE and 14 FMP molecules corresponded to 1 M LiFSI THF2/TTE/FMP electrolyte, and they were randomly inserted into a cube box with a side length of 5.0 nm. The MD simulation was made assuming the temperature was 25℃. The steepest descent method was applied to minimize the initial energy for each system with a force tolerance of 1 kJ/mol nm^{-1} and a maximum step size of 0.002 ps before MD calculations [63]. In all the three directions, periodic boundary conditions were applied. Leapfrog algorithm was used to integrate the Newtonian equation of motion. The MD simulation was processed in an NPT ensemble and the simulation time is 20 ns. In NPT simulations, the pressure was maintained at 1 bar by the Berendsen barostat in an isotropic manner [64] and the temperature was maintained at 298.15 K by the V-rescale thermostat. The Particle-Mesh-Ewald (PME) with a fourth-order interpolation was used to evaluate the electrostatic interactions and whereas a cutoff of 1.0 nm was employed to calculate the short-range van der Waals interactions [65].

4.3. Electrochemical measurements

Three kinds of cells were used in the Electrochemical measurements, including three-electrodes cell, 2032 coin-cell and two-electrodes cell with micro-sized working electrode, and they were all assembled in a glove box filled with Ar atmosphere. The electrolyte amount in each cell was 40 μL unless specified. Cycling tests were conducted on LAND 2001A battery test system. Average CE was measured in the Li/Cu half-cell using standard Aurbach protocol.[49] Linear sweep voltammetry (LSV) was conducted on an electrochemical workstation (Reference600, Gamry USA) to determine the electrochemical window of electrolytes. Three-electrodes cell was used and it was composed of Pt foil working electrode and Li foil reference/counter electrodes, the cell was swept from open circuit voltage (OCV) to 0 V (cathodic sweeping) or 6 V (anodic sweeping) at a scanning rate of 0.2 mV s^{-1}. The electrochemical impedance spectroscopy (EIS) measurements were conducted on Li/Li symmetric cell and Li/LFP full-cell at different temperature using Gamry electrochemical workstation (Reference600, USA). The frequency range was $10^6 \sim 10^{-2}$ Hz and potential amplitude was 5 mV. Ionic conductivity was measured with ion-conductivity meter (Leici, Shanghai, China) after the electrolyte being cooled in the refrigerator for 2 hr. Two kinds of refrigerators were used according to the temperature requirement (DW-HW50 refrigerator, −10 °C ~ − 86 °C, ±2°C, MEILING, China or High/low temperature chamber, −45 °C ~ 200 °C, ±0.1 °C, Soyater, China).

4.4. Other characterizations

The solvation structure and ion diffusion coefficient of electrolytes were analyzed in term of ^7Li spectra and ^1H-^{19}F heteronuclear overhauser effect spectroscopy (HOESY) and diffusion ordered spectroscopy (DOSY), the measurement was conducted on nuclear magnetic resonance spectrometer (NMR, AVANCE NEO, 600 MHz, Bruker) using 0.01 M LiCl D_2O and DMSO-d_6 as the internal standard sealed in the coaxial tube. Raman spectra of electrolyte were obtained on Optosky ATR3200 with 1064 nm laser source. Surface chemistry on anode or cathode was analyzed by X-ray photoelectron spectroscopy (XPS, ESCALAB250Xi, Thermo Fisher Scientific). The morphology was observed through field emission scanning electron microscopy (FE-SEM, Zeiss Merlin Compact). In Cryo-TEM observation, 0.25 mAh cm^{-2}Li was plated on a copper grid with the lacey carbon films (200 mesh) under the current density of 0.5 mA cm^{-2} prior to observation. The microstructure analysis was carried out on transmission electron microscope (TEM, Krios G4,300 kV Field Emission).

CRediT authorship contribution statement

Jian Qin: Writing – review & editing, Writing – original draft, Supervision, Investigation, Data curation. **Yali Zhao:** Investigation. **Xianjiao Meng:** Investigation. **Mengfan Wang:** Investigation. **Zhiping Song:** Supervision. **Xinping Ai:** Supervision. **Hui Zhan:** Writing – review & editing, Writing – original draft, Supervision.

Declaration of competing interest

The authors declare that they have no known competing financial interests or personal relationships that could have appeared to influence the work reported in this paper.

Data availability

Data will be made available on request.

Acknowledgements

The authors acknowledge the financial support from the National Key Research and Development Program (2022YFB2402203). In addition, the authors acknowledge the support from the Core Research Facilities of College of Chemistry and Molecular Sciences for SEM analysis, the Core Facility of Wuhan University for TEM and NMR

characterization, and the Supercomputing Center of Wuhan University for the numerical calculations.

Appendix A. Supplementary data

Supplementary data to this article can be found online at https://doi.org/10.1016/j.cej.2024.153818.

References

[1] M. Armand, J.M. Tarascon, Building better batteries, Nature 451 (2008) 652–657.
[2] B. Dunn, H. Kamath, J.M. Tarascon, Electrical energy storage for the grid: a battery of choices, Science 334 (2011) 928–935.
[3] N. Piao, X. Gao, H. Yang, Z. Guo, G. Hu, H.M. Cheng, F. Li, Challenges and development of lithium-ion batteries for low temperature environments, Etransportation 11 (2022) 100145.
[4] J. Xu, J. Zhang, T.P. Pollard, Q. Li, S. Tan, S. Hou, H. Wan, F. Chen, H. He, E. Hu, K. Xu, X. Yang, O. Borodin, C. Wang, Electrolyte design for Li-ion batteries under extreme operating conditions, Nature 614 (2023) 694–700.
[5] Y. Feng, L. Zhou, H. Ma, Z. Wu, Q. Zhao, H. Li, K. Zhang, J. Chen, Challenges and advances in wide-temperature rechargeable lithium batteries, Energy Environ. Sci. 15 (2022) 1711–1759.
[6] D. Lin, Y. Liu, Y. Cui, Reviving the lithium metal anode for high-energy batteries, Nat. Nanotechnol. 12 (2017) 194–206.
[7] J. Qian, W.A. Henderson, W. Xu, P. Bhattacharya, M. Engelhard, O. Borodin, J. G. Zhang, High rate and stable cycling of lithium metal anode, Nat. Commun. 6 (2015) 6362.
[8] M.D. Tikekar, S. Choudhury, Z. Tu, L.A. Archer, Design principles for electrolytes and interfaces for stable lithium-metal batteries, Nat. Energy 1 (2016) 1–7.
[9] K.N. Wood, M. Noked, N.P. Dasgupta, Lithium metal anodes: toward an improved understanding of coupled morphological, electrochemical, and mechanical behavior, ACS Energy Lett. 2 (2017) 664–672.
[10] X.B. Cheng, R. Zhang, C.Z. Zhao, Q. Zhang, Toward safe lithium metal anode in rechargeable batteries: a review, Chem. Rev. 117 (2017) 10403–10473.
[11] X. Wang, M. Chen, S. Li, C. Zhao, W. Zhang, Z. Shen, Y. He, G. Feng, Y. Lu, Inhibiting dendrite growth via regulating the electrified interface for fast-charging lithium metal anode, ACS Cent. Sci. 7 (2021) 2029–2038.
[12] W. Liu, P. Liu, D. Mitlin, Review of emerging concepts in SEI analysis and artificial SEI membranes for lithium, sodium, and potassium metal battery anodes, Adv. Energy Mater. 2020 (10) (2020) 2002297.
[13] K. Huang, S. Bi, B. Kurt, C. Xu, L. Wu, Z. Li, G. Feng, X. Zhang, Regulation of SEI formation by anion receptors to achieve ultra-stable lithium-metal batteries, Angew. Chem. 133 (2021) 19381–19389.
[14] J.W. Choi, D. Aurbach, Promise and reality of post-lithium-ion batteries with high energy densities, Nat. Rev. Mater. 1 (2016) 1–16.
[15] W. Cao, J. Lu, K. Zhou, G. Sun, J. Zheng, Z. Geng, H. Li, Organic-inorganic composite SEI for a stable Li metal anode by in-situ polymerization, Nano Energy 95 (2022) 106983.
[16] J. Liu, Z. Bao, Y. Cui, E.J. Dufek, J.B. Goodenough, P. Khalifah, Q. Li, B. Liaw, P. Liu, A. Manthiram, Y.S. Meng, V.R. Subramanian, M. Toney, V. Viswanathan, M. S. Whittingham, J. Xiao, W. Xu, J. Yang, X. Yang, J.G. Zhang, Pathways for practical high-energy long-cycling lithium metal batteries, Nat. Energy 4 (2019) 180–186.
[17] S. Zhang, F. Sun, X. Du, X. Zhang, L. Huang, J. Ma, S. Dong, A. Hilger, I. Manke, L. Li, B. Xie, J. Li, Z. Hu, A. Komarek, H. Lin, C. Kuo, C. Chen, P. Han, G. Xu, Z. Cui, G. Cui, In situ-polymerized lithium salt as a polymer electrolyte for high-safety lithium metal batteries, Energy Environ. Sci. 16 (2023) 2591–2602.
[18] X.B. Cheng, R. Zhang, C.Z. Zhao, F. Wei, J.G. Zhang, Q. Zhang, A review of solid electrolyte interphases on lithium metal anode, Adv. Sci. 3 (2016) 1500213.
[19] J. Liu, B. Yuan, N. He, L. Dong, D. Chen, S. Zhong, Y. Ji, J. Han, C. Yang, Y. Liu, W. He, Reconstruction of LiF-rich interphases through an anti-freezing electrolyte for ultralow-temperature $LiCoO_2$ batteries, Energy Environ. Sci. 16 (2023) 1024–1034.
[20] M.S. Kim, Z. Zhang, J. Wang, S.T. Oyakhire, S.C. Kim, Z. Yu, Y. Chen, D. Boyle, Y. Ye, Z. Huang, W. Zhang, R. Xu, P. Sayavong, S. Bent, J. Qin, Z. Bao, Y. Cui, Revealing the multifunctions of Li_3N in the suspension electrolyte for lithium metal batteries, ACS Nano 17 (2023) 3168–3180.
[21] J. Ko, Y.S. Yoon, Recent progress in LiF materials for safe lithium metal anode of rechargeable batteries: is LiF the key to commercializing Li metal batteries? Ceram. Int. 45 (2019) 30–49.
[22] M.M. Rahman, S. Tan, Y. Yang, H. Zhong, S. Ghose, I. Waluyo, A. Hunt, L. Ma, X. Yang, E. Hu, An inorganic-rich but LiF-free interphase for fast charging and long cycle life lithium metal batteries, Nat. Commun. 14 (2023) 8414.
[23] S. Ye, X. Chen, R. Zhang, Y. Jiang, F. Huang, H. Huang, Y. Yao, S. Jiao, X. Chen, Q. Zhang, Y. Yu, Revisiting the role of physical confinement and chemical regulation of 3D hosts for dendrite-free Li metal anode, Nanomicro Lett. 14 (2022) 187.
[24] P. Pathak, K. Chen, A. Gurung, K.M. Reza, B. Bahrami, J. Pokharel, A. Baniya, W. He, F. Wu, Y. Zhou, K. Xu, Q. Qiao, Fluorinated hybrid solid-electrolyte-interphase for dendrite-free lithium deposition, Nat. Commun. 11 (2020) 93.
[25] X. Cao, P. Gao, X. Ren, L. Zou, M.H. Engelhard, B.E. Matthews, J. Hu, C. Niu, D. Liu, B. Arey, C. Wang, J. Xiao, J. Liu, W. Xu, J.G. Zhang, Effects of fluorinated solvents on electrolyte solvation structures and electrode/electrolyte interphases for lithium metal batteries, Proc. Natl. Acad. Sci. 118 (2021) e2020357118.
[26] C. Cui, C. Yang, N. Eidson, J. Chen, F. Han, L. Chen, C. Luo, P. Wang, X. Fan, C. Wang, A highly reversible, dendrite-free lithium metal anode enabled by a lithium-fluoride-enriched interphase, Adv. Mater. 32 (2020) 1906427.
[27] C.V. Amanchukwu, Z. Yu, X. Kong, J. Qin, Y. Cui, Z. Bao, A new class of ionically conducting fluorinated ether electrolytes with high electrochemical stability, J. Am. Chem. Soc. 142 (2020) 7393–7403.
[28] X. Ren, L. Zou, X. Cao, M.H. Engelhard, W. Liu, S.D. Burton, H. Lee, C. Niu, B. Matthews, Z. Zhu, C. Wang, B. Arey, J. Xiao, J. Liu, J.G. Zhang, W. Xu, Enabling high-voltage lithium-metal batteries under practical conditions, Joule 3 (2019) 1662–1676.
[29] X. Meng, J. Qin, Y. Liu, Z. Liu, Y. Zhao, Z. Song, H. Zhan, Electrolyte strategy toward the low-temperature Li-metal secondary battery, Chem. Eng. J. 465 (2023) 142913.
[30] M. Mao, X. Ji, Q. Wang, Z. Lin, M. Li, T. Liu, C. Wang, Y. Hu, H. Li, X. Huang, L. Chen, L. Suo, Anion-enrichment interface enables high-voltage anode-free lithium metal batteries, Nat. Commun. 14 (2023) 1082.
[31] J. Zhang, Q. Li, Y. Zeng, Z. Tang, D. Sun, D. Huang, Y. Tang, H. Wang, Weakly solvating cyclic ether electrolyte for high-voltage lithium metal batteries, ACS Energy Lett. 8 (2023) 1752–1761.
[32] P. Li, W. Feng, X. Dong, Y. Wang, Y. Xia, A new strategy of constructing a highly fluorinated solid-electrolyte interface towards high-performance lithium anode. Adv. Mater. Interfaces, 7, 2000154.
[33] R. Cao, J. Chen, K.S. Han, W. Xu, D. Mei, P. Bhattacharya, M. Engelhard, K. Mueller, J. Liu, J.G. Zhang, Effect of the anion activity on the stability of Li metal anodes in lithium-sulfur batteries, Adv. Funct. Mater. 26 (2016) 3059–3066.
[34] C.V. Amanchukwu, X. Kong, J. Qin, Y. Cui, Z. Bao, Nonpolar alkanes modify lithium-ion solvation for improved lithium deposition and stripping, Adv. Energy Mater. 9 (2019) 1902116.
[35] X.Q. Zhang, X.B. Cheng, X. Chen, C. Yan, Q. Zhang, Fluoroethylene carbonate additives to render uniform Li deposits in lithium metal batteries, Adv. Funct. Mater. 27 (2017) 1605989.
[36] X. Fan, L. Chen, O. Borodin, X. Ji, J. Chen, S. Hou, T. Deng, J. Zheng, C. Yang, S. Liou, K. Amine, K. Xu, C. Wang, Non-flammable electrolyte enables Li-metal batteries with aggressive cathode chemistries, Nat. Nanotechnol. 13 (2018) 715–722.
[37] X. Liu, M. Zarrabeitia, A. Mariani, X. Gao, H.M. Schütz, S. Fang, T. Bizien, G. Elia, S. Passerini, Enhanced Li^+ transport in ionic liquid-based electrolytes aided by fluorinated ethers for highly efficient lithium metal batteries with improved rate capability, Small Methods 5 (2021) 2100168.
[38] M.R. Bauer, M.D. Mackey, Electrostatic complementarity as a fast and effective tool to optimize binding and selectivity of protein-ligand complexes, J. Med. Chem. 62 (2019) 3036–3050.
[39] Y. Wu, Q. Hu, H. Liang, A. Wang, H. Xu, L. Wang, X. He, Electrostatic potential as solvent descriptor to enable rational electrolyte design for lithium batteries, Adv. Energy Mater. (2023) 2300259.
[40] D. Ruan, L. Tan, S. Chen, J. Fan, Q. Nian, L. Chen, Z. Wang, X. Ren, Solvent versus anion chemistry: unveiling the structure-dependent reactivity in tailoring electrochemical interphases for lithium-metal batteries, JACS Au 3 (2023) 953–963.
[41] K. Xu, Nonaqueous liquid electrolytes for lithium-based rechargeable batteries, Chem. Rev. 104 (2004) 4303–4418.
[42] K. Kimura, J. Motomatsu, Y. Tominaga, Correlation between solvation structure and ion-conductive behavior of concentrated poly (ethylene carbonate)-based electrolytes, J. Phys. Chem. C 120 (2016) 12385–12391.
[43] A. Lahiri, T. Schubert, B. Iliev, F. Endres, LiTFSI in 1-butyl-1-methylpyrrolidinium bis(fluorosulfonyl)amide: a possible electrolyte for ionic liquid-based lithium-ion batteries, Phys. Chem. Chem. Phys. 17 (2015) 11161–11164.
[44] C. Efaw, Q. Wu, N. Gao, Y. Zhang, H. Zhu, K. Gering, M. Hurley, H. Xiong, E. Hu, X. Cao, W. Xu, J. Zhang, E. Dufek, J. Xiao, X. Yang, J. Liu, Y. Qi, B. Li, Localized high-concentration electrolytes get more localized through micelle-like structures, Nature Materials 22 (2023) 1531–1539.
[45] S. Kim, J. Lee, T. Lee, K. Baek, J. Kim, B. Kim, J. Byun, H. Lee, S. Kang, J. Choi, S. Lee, M. Choi, J. Lee, N. Choi, Wide-temperature-range operation of lithium-metal batteries using partially and weakly solvating liquid electrolytes, Energy Environ. Sci. 16 (2023) 5108–5122.
[46] X. Cao, X. Ren, L. Zou, M.H. Engelhard, W. Huang, H. Wang, B. Matthews, H. Lee, C. Niu, B. Arey, Y. Cui, C. Wang, J. Xiao, J. Liu, W. Xu, J.G. Zhang, Monolithic solid-electrolyte interphases formed in fluorinated orthoformate-based electrolytes minimize Li depletion and pulverization, Nat. Energy 4 (2019) 796–805.
[47] J. Xiao, How lithium dendrites form in liquid batteries, Science 366 (2019) 426–427.
[48] W. Martin, Y. Tian, J. Xiao, Understanding diffusion and electrochemical reduction of Li^+ ions in liquid lithium metal batteries, J. Electrochem. Soc. 168 (2021) 060513.
[49] B.D. Adams, J. Zheng, X. Ren, W. Xu, J.G. Zhang, Accurate determination of coulombic efficiency for lithium metal anodes and lithium metal batteries, Adv. Energy Mater. 8 (2018) 1702097.
[50] S. Chen, Y. Xiang, G. Zheng, Y. Liao, F. Ren, Y. Zheng, H. He, B. Zheng, X. Liu, N. Xu, M. Luo, J. Zheng, Y. Yang, High-efficiency lithium metal anode enabled by a concentrated/fluorinated ester electrolyte, ACS Appl. Mater. Interfaces 12 (2020) 27794–27802.
[51] S. Wang, J. Qu, F. Wu, K. Yan, C. Zhang, Cycling performance and kinetic mechanism analysis of a Li metal anode in series-concentrated ether electrolytes, ACS Appl. Mater. Interfaces 12 (2020) 8366–8375.

[52] J. Holoubek, H. Liu, Z. Wu, Y. Yin, X. Xing, G. Cai, S. Yu, H. Zhou, T. Pascal, Z. Chen, P. Liu, Tailoring electrolyte solvation for Li metal batteries cycled at ultra-low temperature, Nat. Energy 6 (2021) 303–313.
[53] X. Dong, Y. Lin, P. Li, Y. Ma, J. Huang, D. Bin, Y. Wang, Y. Qi, Y. Xia, High-energy rechargeable metallic lithium battery at −70°C enabled by a cosolvent electrolyte, Angew. Chem. Int. Ed. 58 (2019) 5623–5627.
[54] C.S. Rustomji, Y. Yang, T.K. Kim, J. Mac, Y.J. Kim, E. Caldwell, H. Chung, Y. S. Meng, Liquefied gas electrolytes for electrochemical energy storage devices, Science 356 (2017) eaal4263.
[55] J. Holoubek, K. Kim, Y. Yin, Z. Wu, H. Liu, M. Li, A. Chen, H. Gao, G. Cai, T. Pascal, P. Liu, Z. Chen, Electrolyte design implications of ion-pairing in low-temperature Li metal batteries, Energy Environ. Sci. 15 (2022) 1647–1658.
[56] T. Lu, F. Chen, Multiwfn: A multifunctional wavefunction analyzer, J. Comput. Chem. 33 (2012) 580–592.
[57] S. Manzetti, T. Lu, The geometry and electronic structure of Aristolochic acid: possible implications for a frozen resonance, J. Phys. Org. Chem. 26 (2013) 473–483.
[58] C.G. Zhan, J.A. Nichols, D.A. Dixon, Ionization potential, electron affinity, electronegativity, hardness, and electron excitation energy: molecular properties from density functional theory orbital energies, J. Phys. Chem. A 107 (2003) 4184–4195.
[59] D. Spoel, E. Lindahl, B. Hess, G. Groenhof, A. Mark, H. Berendsen, GROMACS: Fast, flexible, and free, J. Comput. Chem. 26 (2005) 1701–1718.
[60] G.A. Petersson, M.A. Al-Laham, A complete basis set model chemistry. II. Open-shell systems and the total energies of the first-row atoms, J. Chem. Phys. 94 (1991) 6081–6090.
[61] W.L. Jorgensen, D.S. Maxwell, J. Tirado-Rives, Pdb2gmx for topology file, J. Am. Chem. Soc. 118 (1996) 11225–11236.
[62] R. de Lima, K. Coutinho, Classical force field for dialkylaniline photosensitive dyes. Center for Innovation on New Energies, 36.
[63] W.F. Van Gunsteren, H. Berendsen, A leap-frog algorithm for stochastic dynamics, Mol. Simul. 1 (1988) 173–185.
[64] B. Hess, H. Bekker, H.J. Berendsen, J.G. Fraaije, LINCS: A linear constraint solver for molecular simulations, J. Comput. Chem. 18 (1997) 1463–1472.
[65] T. Darden, D. York, L. Pedersen, The effect of long-range electrostatic interactions in simulations of macromolecular crystals–a comparison of the ewald and truncated list methods, J. Chem. Phys. 98 (1993) 10089.